UC Riverside

UC Riverside Previously Published Works

Title

Theoretical insights on potential-dependent oxidation behaviors and antioxidant strategies of MXenes.

Permalink

https://escholarship.org/uc/item/6qk84152

Journal

Nature Communications, 15(1)

Authors

Tian, Yumiao
Hou, Pengfei
Zhang, Huiwen
et al.

Publication Date

2024-11-21

DOI

10.1038/s41467-024-54455-z

Peer reviewed

Theoretical insights on potential-dependent oxidation behaviors and antioxidant strategies of MXenes

Yumiao Tian [1,2], Pengfei Hou[1,2], Huiwen Zhang [1], Yu Xie[2], Gang Chen[1], Quan Li [2,3] ✉, Fei Du [1] ✉, Aleksandra Vojvodic [4] ✉, Jianzhong Wu [5] ✉ & Xing Meng [1,2,4] ✉

Significant efforts have been devoted to investigating the oxidation of MXenes in various environments. However, the underlying mechanism of MXene oxidation and its dependence on the electrode potential remain poorly understood. Here we show the oxidation behavior of MXenes under the working conditions of electrochemical processes in terms of kinetics and thermodynamics by using constant-potential ab initio simulations. The theoretical results indicate that the potential effects can be attributed to the nucleophilic attack of water molecules on metal atoms, similar to that taking place in the Oxygen Evolution Reaction. Building upon these findings, we deduced the oxidation potential of the common MXenes, and proposed antioxidant strategies for MXene. Finally, we demonstrated that MBenes, the boron analogs of MXenes, may undergo a similar nucleophilic attack in water and inferred that molecule-induced Walden inversion is widely present in material reconstructions. This work contributes to a fundamental understanding MXene stability at the atomic level, and promotes the transition in materials discovery from trial-and-error synthesis to rational design.

MXenes are two-dimensional transition metal carbides and nitrides, constituting probably the largest family of two-dimensional materials. While extensive applications have been proposed in fields such as energy, devices, and medicine, a common concern is whether MXenes undergo oxidative degradation due to interactions with the surroundings[1]. Maintaining the stability of MXenes is crucial, in particular for their integration into medical platforms and devices[2]. A comprehensive understanding of the oxidation mechanism of MXenes is also important from the perspective of materials synthesis. In certain cases, their performance requires the controlled oxidation of MXenes to enhance the overall properties. For example, metal-oxide composites, such as $TiO_2/Ti_3C_2T_x$, Nb_2O_5/Nb_2CT_x, $Nb_2O_5/Nb_4C_3T_x$, and V_2O_x/V_2CT_x,

can be constructed through oxidation. The materials can significantly improve electrode cycling stability compared to pristine MXenes[3,4].

In recent years, significant progress has been made in understanding MXene oxidation, encompassing both experimental and theoretical approaches. Experimental studies have demonstrated the pivotal role of water molecules in MXene oxidation and proposed methods such as low-temperature oxygen isolation and the addition of ascorbic acid[5-7]. Meanwhile, theoretical investigations also provide a dynamic description description of water molecules attacking on the surface of MXenes[8-11].

However, in practical applications, such as electrocatalysis, batteries, and supercapacitors, MXenes do not exist in their ideal storage

[1]Key Laboratory of Physics and Technology for Advanced Batteries (Ministry of Education), College of Physics, Jilin University, Changchun, China. [2]Key Laboratory of Material Simulation Methods & Software of Ministry of Education, College of Physics, Jilin University, Changchun, China. [3]International Center of Future Science, Jilin University, Changchun, China. [4]Department of Chemical and Biomolecular Engineering, University of Pennsylvania, Philadelphia, PA, United States of America. [5]Department of Chemical and Environmental Engineering, University of California, Riverside, CA, United States of America. ✉e-mail: liquan777@jlu.edu.cn; dufei@jlu.edu.cn; alevoj@seas.upenn.edu; jwu@engr.ucr.edu; mengxing@jlu.edu.cn

conditions. Under these circumstances, the oxidation of MXenes is distinctly correlated with the electrode potential, a critical factor that is often ignored in previous studies. For example, $Ti_3C_2T_x$ electrode will be easily oxidized beyond $0.1-0.2$ V vs. Ag/AgCl[12–14], and V_2CT_x exhibits noticeable oxidation in cyclic voltammetry tests[15,16]. Understanding what happens to MXenes under the working conditions of electrochemical processes is imperative to both the application and development of MXene materials. But previous theoretical studies have primarily focused on the superficial phenomenon of water molecule attacks on MXenes. They have not adequately addressed deeper aspects such as the electronic changes during the attack, the potential-dependent oxidation behavior, and the implications of this potential dependency for practical applications.

In this work, we employ the "constant-potential hybrid-solvation dynamic model" (CP-HS-DM)[17–19] and constant-potential implicit solvent models[20] to study the oxidation behavior of MXenes in an oxygen-containing aqueous environment from both dynamic and thermodynamic perspectives. The dynamic analysis revealed that MXene oxidation is influenced by the potential due to the nucleophilic attack of water molecules on metal atoms, resembling the Oxygen Evolution Reaction (OER). Through thermodynamic analysis, we obtained the oxidation potential of MXenes and identified key factors influencing MXenes oxidation under electrochemical working conditions, thereby proposing antioxidation strategies. We also demonstrate that MBenes[21–23], the boron analogs of MXenes, may undergo a similar nucleophilic attack in water.

Results

Unconstrained AIMD simulations of MXene oxidation in pure water and oxygen-containing environments

We first explore the oxidation behavior of MXenes in different environments by constructing confined environments with liquid water, both with and without an oxygen molecule. The structural configurations are illustrated in Supplementary Fig. S1a. Compared to the common $Ti_3C_2T_x$, it has been experimentally observed that V_2CT_x is more prone to oxidation[24], and the degradation process of MXenes is similar in a humid environment[8–10]. Therefore, V_2CO_2 is chosen as the main research object. An unconstrained AIMD simulation was carried out at 300 K for 50 ps.

The simulation results reveal that, in pure water (Fig. 1a), V_2CO_2 undergoes nucleophilic attack by water molecules within about 1.430 ps. To simplify the discussion and distinguish different sources of oxygen atoms involved in the oxidation process, we use different subscripts: O_W stands for the oxygen atom from an attacking water molecule, and O_M for the oxygen from a functional group in MXene. The water molecule is able to form a chemical bond with a V atom at the MXene surface, similar to an S_N2 reaction in organic chemistry. The attacked V atom undergoes Walden inversion, separating from the C layer of the MXene. During this process, the attacking water molecule is deprotonated, forming a protruding $V\text{-}O_WH$ structure. The key oxidation steps of this process are shown in Fig. 1c. Around 1.521 ps, deprotonation occurs again, resulting in a $V\text{-}O_W$ structure. At ~38.580 ps, a second water molecule begins to attack the V atom, followed by a third deprotonation.

To investigate the stability of V oxides in a pure water environment, we conducted AIMD simulations at 1000 K. It was found that the V oxides eventually stabilized on the surface in an octahedral form, following three deprotonation steps (Supplementary Fig. S2). We also conducted AIMD simulations for $Ti_3C_2O_2$ in pure water at 1000 K (Supplementary Fig. S3). Aligned with previous studies[9,10], the results indicate that simulation at high temperature effectively accelerates the oxidation process. $Ti_3C_2O_2$ exhibits a pattern of water attack very similar to V_2CO_2. However, notably, in the process of $Ti_3C_2O_2$ being attacked, water molecules undergo deprotonation only once.

Oxygen-related reactions, such as the oxygen evolution/reduction reaction, have important applications in energy fields such as catalysis and fuel cells. Therefore, it is necessary to consider the presence of oxygen in the environment. The oxidation of MXenes in an oxygen-containing environment is illustrated in Fig. 1b, which includes one oxygen molecule. The water attack occurs within about 0.556 ps, similar to that in pure water, leading to the formation of the protruding $V\text{-}O_W$ structure. Unlike oxygen atoms in water molecules, oxygen molecules are nonpolar and thus have difficulty attacking metal atoms protected by functional groups, as shown in Supplementary Fig. S4. This explains why MXene is more stable in a pure oxygen environment than in water[5]. However, for the $V\text{-}O_W$ structure protruding from the surface, the V atom loses the protection of functional groups. Figure 1b
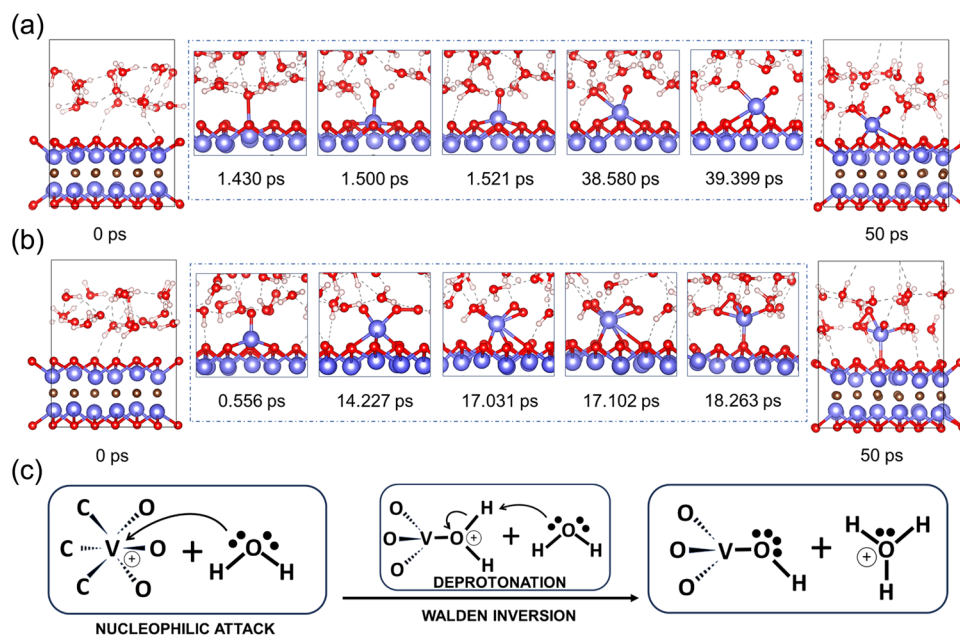

Fig. 1 | Snapshots from unconstrained dynamic simulations of V_2CO_2 oxidation. a Pure water and (**b**) oxygen-containing environments. **c** Schematic of the key oxidation steps. V: purple; C: brown; O: red; H: white.

shows that V-O_W is attacked by O_2 at about 14.227 ps, and subsequently, it undergoes a nucleophilic attack from a second water molecule around 17.031 ps. At this point, the V-O_M bonds in the MXene begin to break, exposing the C layer through the opening of vacancies and forming V oxide suspended on the surface. This observation underscores the highly promotive role of O_2 in the MXene oxidation process, aligning well with experimental findings[25].

Through the energy analysis of the reaction process (Supplementary Fig. S5), we identified three processes that cause significant energy changes: the first water molecule attack, the oxygen molecule attack, and the vacancy opening. The vacancy opening is not a molecular attack process but rather a spontaneous surface reconstruction. Therefore, we propose that MXene oxidation takes place in two key stages: first, the nucleophilic attack of water molecules on metal atoms, forming the protruding V-O_W structure; and second, the subsequent attack of oxygen molecules and the rupture of V-O_M bonds. Next, we will explore the potential dependency of MXene oxidation through these two reaction steps.

Constrained AIMD simulation of water's nucleophilic attack on metal atoms

To obtain the variation of free energy during the reaction process under working conditions, we carried out MD simulation using the CP-HS-DM. All simulated temperatures not otherwise stated below are 300 K. The slow-growth approach is implemented to collect the free energy along the reaction path. The model, principles, and the choice of collective variables (CV) used in this section are described in Supplementary Fig. S1b, the "Methods" section, and Supplementary Fig. S6a, respectively. The forces during the sampling process are shown in Supplementary Fig. S7. Since MXenes undergo oxidation spontaneously in their natural state but are stable at low applied electrode potentials[14,26], we simulated the open-circuit (OC) state (the natural state without an applied external potential) and the state with an electrode potential of 0 V to explore the relationship between surface potential and MXenes oxidation. Figure 2 compares the water nucleophilic attack process under these two different states.
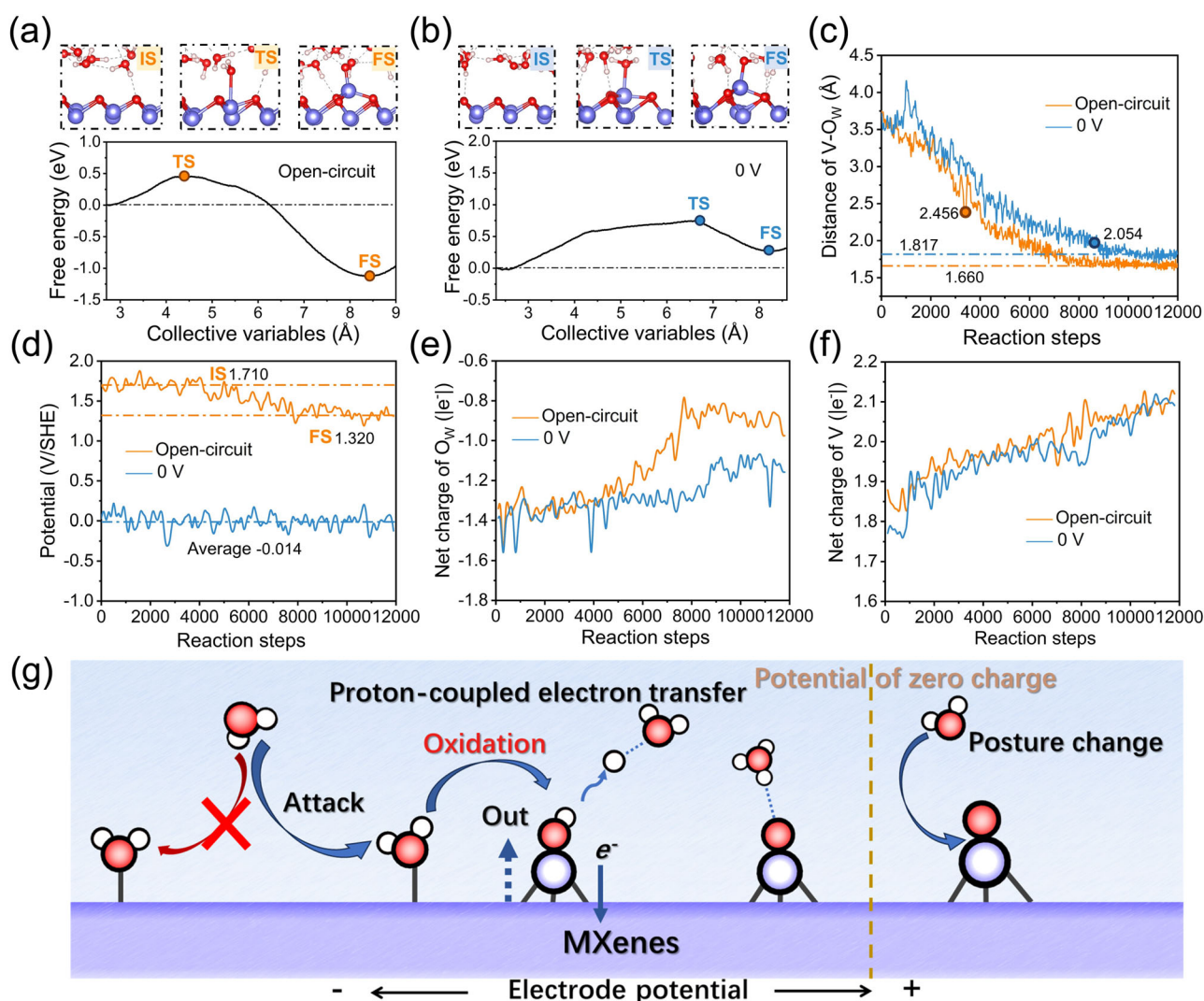

Fig. 2 | Reaction mechanism for the potential-dependent MXene oxidation in Water. Free energy profile during the process of V atom being attacked by water under the condition of (**a**) open-circuit and (**b**) zero electrode potential (U = 0 V). The structures at the initial state (IS), transition state (TS), and final state (FS) are shown at the top of the figures. The following evolutions throughout the reaction are depicted in Figure (**c**–**f**): (**c**) distance between V and O_W atoms, where dots indicate the TS position and the dash-dot lines represent the V-O_W bond length at FS; (**d**) system potential relative to the standard hydrogen electrode (SHE), with the yellow dash-dot lines indicating the potential at IS and FS under the open-circuit condition and the blue dash-dot line marking the average potential during the 0 V simulation; (**e**) net charge of O_W atom; and (**f**) net charge of the V atom. **g** Schematic diagram of potential-dependent MXene oxidation in water. Source data are provided as a Source Data file.

The reaction dynamics under the OC state is illustrated in Fig. 2a and c. The free energy increases at the start of the reaction, reaching a reaction barrier of 0.451 eV when the V-O_W distance is 2.456 Å. As the reaction further progresses, proton dissociation occurs spontaneously (Supplementary Fig. S8a), as evidenced by the reduction of the free energy. When the V-O_W distance is 1.66 Å, the free energy drops to −1.125 eV, signaling the formation of the V-O_W structure. Under the condition of 0 V, as shown in Fig. 2b and c, the free energy profile is significantly increased. Proton dissociation initiates after the energy barrier reaches 0.744 eV at a V-O_W distance of 2.054 Å (Supplementary Fig. S8b). The oxidation reaction attains its final state when the V-O_W distance is 1.817 Å, with a free energy of 0.269 eV. Notably, only one proton is released throughout the process, ultimately forming the V-O_WH structure. The longer V-O_W bond lengths in the transition state and final state, combined with less deprotonation, indicate that a low potential hinders the reaction progression and outcome. Clearly, MXene oxidation is an electrochemical process regulated by the potential.

Next, we explore the reasons why the free energy is influenced by the applied electrode potential at both the transition state and the final state. To identify the factors influencing the free-energy change, we performed simulations for the reaction process at U = 2.0 V and analyzed the orientation distribution of water molecules in the inner Helmholtz plane under a wide range of conditions (Supplementary Fig. S9). We found that the electrode potential significantly alters the orientation of water molecules. At low potential, the water molecules tend to align with their dipoles pointing toward the basal plane (H-down), making the O_W atoms difficult to get close to the surface for nucleophilic reactions. Conversely, at high potential, the water molecules tend to align with O_W-down, facilitating their attack on metal atoms. Furthermore, regardless of the potential, after the formation of the V-O_W structure, we observed that the orientation of the water molecules changed from O_W-down to H-down. This suggests that the V-O_W structure hinders the subsequent attack of water molecules on metal atoms at the surface. Additionally, the potential also affects charge distribution of each atomic layer in MXenes (Supplementary Fig. S10). The low potential reduces the positive charge of the metal layer and enhances the negative charge of the functional group, making the nucleophilic attack of water molecules difficult. Therefore, lowing the electrode potential can increase the reaction barrier, impeding reaction progress.

The change in the final state free energy can also be analyzed from the perspective of electron transfer. As shown in Fig. 2d for MXene oxidation at the OC state, the system potential continuously reduces from the initial state of 1.701 V to the final state of 1.320 V, indicating electron injection into the MXene. The Bader charge analysis (Supplementary Fig. S8c−e) confirms this observation, which is evident in the loss of electrons from both O_w and the attacked V atoms. Under the OC condition, the net charge of O_W (Fig. 2e) at the final state is -0.852 |e|, and under U = 0 V, it is -1.115 |e|. Clearly, the different potentials lead to different oxidation states of O_W atoms. Interestingly, the V atom maintains a consistent net charge of approximately 2.1 |e| under both OC and 0 V conditions, suggesting that the potential influences the oxidation degree of O_W rather than MXene. Regardless of the potential, V atoms are oxidized to the same extent, approximately in the positive pentavalent state (Supplementary Table. S1), consistent with experimental measurements[27].

The above analysis indicates that the process of MXene being attacked by water involves the oxidation of O atoms (electron transfer) and proton generation (proton transfer). The relationship between the entire process and potential is shown in Fig. 2g. The proton-coupled electron transfer (PCET) process can be understood by considering the attacked V atom as the dynamic reaction site and using *O to represent V_2CO_2 with the V-O_W structure. In essence, the reaction can be represented by the following equation:

$$H_2O + *(MXene) \rightarrow *O + 2(H^+ + e^-) \tag{1}$$
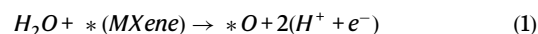
In terms of reaction kinetics, the reaction should be divided into two processes:

$$H_2O + *(MXene) \rightarrow *OH + H^+ + e^- \rightarrow *O + 2(H^+ + e^-) \tag{2}$$
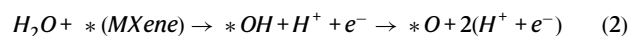
Hence, the relationship between water attacking MXenes and the OER becomes evident. The involvement of electrons (e^-) in the reaction equation signifies the influence of the applied electrode potential and explains why MXene is highly stable at low potential. We used the OER-like reaction pathway (Supplementary Fig. S6b) to resample the process of water attacking V_2CO_2 under OC conditions. The results (Supplementary Fig. S11a) were consistent with previous findings, confirming the accuracy of this reaction pathway. We also performed the process of water attacking $Ti_3C_2O_2$ using the same pathway under OC conditions (Supplementary Fig. S11b). It was observed that the final state of $Ti_3C_2O_2$ has a free energy about 0.2 eV higher than the initial state, indicating that $Ti_3C_2O_2$ is more stable than V_2CO_2. Additionally, through unconstrained AIMD simulations, we found that the oxidized portion of $Ti_3C_2O_2$ is reduced back to a perfect surface at 0 V around 1 ps (Supplementary Fig. S12). This indicates that, under low potential conditions, a certain degree of MXene oxidation is reversible.

Constrained AIMD simulation for the subsequent oxygen attack

We employed the enhanced sampling method to analyze the subsequent attack of oxygen molecules on V oxides at OC and 0 V conditions in oxygen-containing environments (Supplementary Fig. S6c). The forces during the sampling process are shown in Supplementary Fig. S13. Since oxygen molecules are nonpolar and difficult to react with metal atoms protected by the functional groups, our analysis starts with the protruding V oxide (V-O_WH) as the initial state. As shown in Fig. 3a, b, under the OC condition, the reaction barrier is only 0.026 eV, and the free energy at the final state is −0.610 eV. During the reaction, water molecules attack V atoms spontaneously, accompanied by proton detachment to form V-O-OH-OOH. We have conducted additional simulations to demonstrate that spontaneous water molecule adsorption during this process does not affect the sampling results, as shown in Supplementary Fig. S14. Under 0 V, the reaction barrier is 0.115 eV. Subsequently, as the V-OO bond length shortens, it reaches a final state with a free energy of -0.565 eV. No attack by water molecules was observed during the process, and there was no proton detachment. The free energy diagram suggests that oxygen molecules attack V-O_WH spontaneously, little impacted by the potential.

Based on the results from unconstrained AIMD simulations (Fig. 1b and Supplementary fig. S5b), surface reconstruction occurs spontaneously after the O_2 attack. Therefore, we used the final state structure as the input to conduct 2 ps unconstrained AIMD simulation, as shown in Fig. 3c, d. In the OC case, two out of the three V-O_M bonds experienced fluctuations of -0.8 Å. Around 1.2 ps, these two V-O_M bonds broke completely, leaving only one V-O_M bond connecting the V oxide to the MXene surface. In line with our previous simulations, the surface loses the protection of oxides. In the 0 V case, around 0.5 ps, a water molecule adsorbed onto the V atom without proton detachment, forming the V-OH-OH2-OO structure. Eventually, all three V-O_M bonds were stabilized at around 2 Å, and the V oxide on the MXene surface maintained a stable octahedral coordination structure.

In summary, spontaneous interactions of V oxides with water molecules were observed throughout the entire simulation of the oxygen attack. While two protons were detached from V oxide (V-O_WH) under the OC condition, the deprotonation process did not take place under 0 V. The more the desorption of protons, the less stable the oxide, indicating a close association between the stability of V
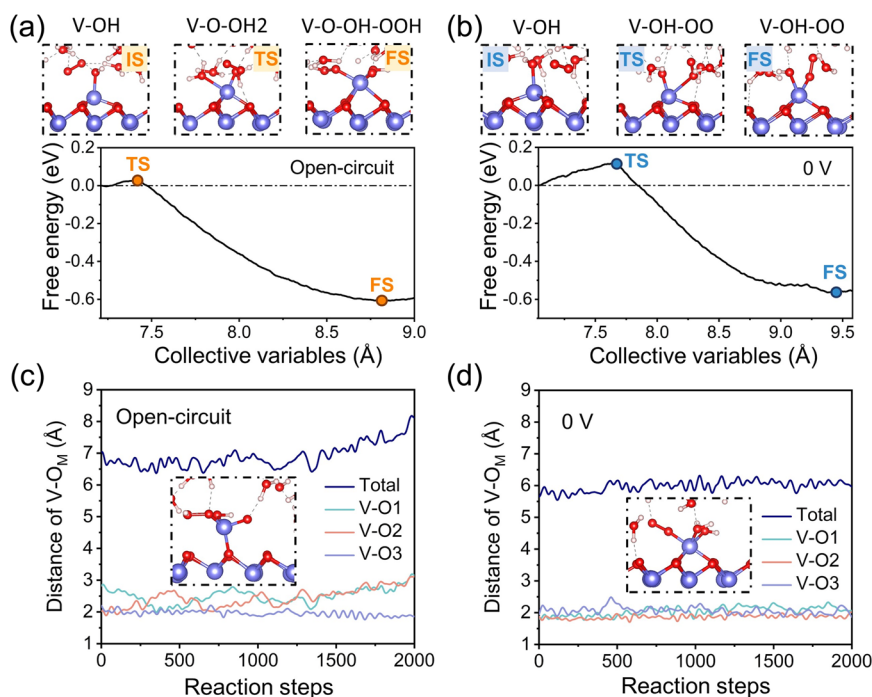
Fig. 3 | Kinetic analysis of the subsequent oxygen attack. Free energy profile for the subsequent reaction of the protruding V oxide with oxygen molecule under (**a**) open-circuit and (**b**) 0 V. The structures at the initial state (IS), transition state (TS), and final state (FS) are displayed above in the Figure. The change of V-O$_M$ distance during 2 ps unconstrained dynamic simulations under (**c**) open-circuit and (**d**) 0 V potential. The total refers to the sum of the three V-O$_M$ bond lengths. The snapshot displays the simulated final state. Source data are provided as a Source Data file.

oxide and proton detachment. From an energetic perspective, the reaction of V oxide with oxygen molecules is less sensitive to the applied potential than the PCET steps. A low potential hinders the PCET process and hydrogen detachment, thereby ultimately promoting the stability of V oxide. This suggests that, in an oxygen-containing environment, the stability of the metal oxide is similarly primarily governed by the nucleophilic attack of water.

The relationship between MXenes oxidation and applied electrode potential

Thus far, we have identified the nucleophilic attack of water molecules as the crucial step leading to MXenes oxidation. Furthermore, we demonstrated that this process is an OER-like reaction. Next, we search for the relationship between MXenes oxidation and the electrode potential. Supplementary Fig. S15 presents the structural models used for the investigation of the potential dependence of the OER-like reaction process. The double-reference method[28] was adopted to simulate the energetics of MXene surfaces ("Methods" section). The chemical potential of the solvated proton and electron pair ($H^+ + e^-$) is calculated as $\frac{1}{2}G_{H2} + eU_{SHE}$ at standard conditions. As the potential increases, the grand canonical free energy of the system during oxidation changes as follow:

$$G_U(slab) + G(H_2O) \rightarrow G_U(*OH) + \frac{1}{2}G(H_2) + eU_{SHE} \rightarrow G_U(*O) + G(H_2) + 2eU_{SHE}$$

$$(3)$$

Figure 4a presents the energy-potential relationship for V$_2$CO$_2$, referenced to the Standard Hydrogen Electrode (SHE) scale. All energy−potential points exhibit a well-fitted quadratic trend. Detailed parameters from the fitting process are provided in Supplementary Table S2. Combining the reaction mechanism and using $G_U(slab) + G(H_2O)$ as the reference state, according to Eq. 3, we can derive the grand canonical free energy curves for each part of the reaction, as shown in Fig. 4b. The equilibrium potential (oxidation potential) for the first proton detachment process is -0.217 V. The MXene tends to maintain a stable surface when the electrode potential is below this equilibrium potential. When the electrode potential is higher than this equilibrium potential, the MXene is prone to oxidation due to the protruding structure. The equilibrium potential for the second proton detachment process is 0.625 V, explaining why, in previous simulations, only the V-O$_W$H structure was generated at 0 V.

To derive a general trend, we also investigated the relationship between the oxidation behavior with the electrode potential for Ti$_3$C$_2$, one of the most extensively studied MXenes. Figure 4c shows the fitted energy−potential functions for each part. The potential of zero charge (PZC) for Ti$_3$C$_2$O$_2$ in water, obtained through fitting, is 1.088 V, with a surface capacitance of 1.465 e/V (32.910 μF/cm^2). These values are consistent with previous studies[29], thereby validating our simulation protocols. Compared to V$_2$CO$_2$, Ti$_3$C$_2$O$_2$ has a weaker OH adsorption energy, as shown in Supplementary Fig. S16, hence exhibiting a higher oxidation potential. The grand canonical free energy curves for Ti$_3$C$_2$O$_2$ oxidation are depicted in Fig. 4d, showing an oxidation potential of 1.329 V. This potential is similar to the experimentally obtained irreversible oxidation peak (1.094 V vs. SHE, pH = 0)[14]. However, the oxidation potentials reported in some studies are significantly lower than our theoretical values[12,13]. We speculate that the discrepancy might be caused by defects or oxygen-containing species in the C layer[30]. Supplementary Fig. S17 confirms this, indicating a potential decrease of almost 1 V due to these factors.

Supplementary Figs. S18 and S19 show the effect of defects in the metal layer on the oxidation of MXenes, only about 0.1 V. However, water tends to attack the metal atoms around the defects, leading to the expansion of defects. It should also be noted that defects often facilitate metal deposition, responsible for the formation of "micro-batteries" that accelerate electrochemical corrosion and cause mechanical damage. As oxidation progresses, the defect expansion leads to the exposure of the carbon layer. Because of the unknown implications for material stability and performance, further research is
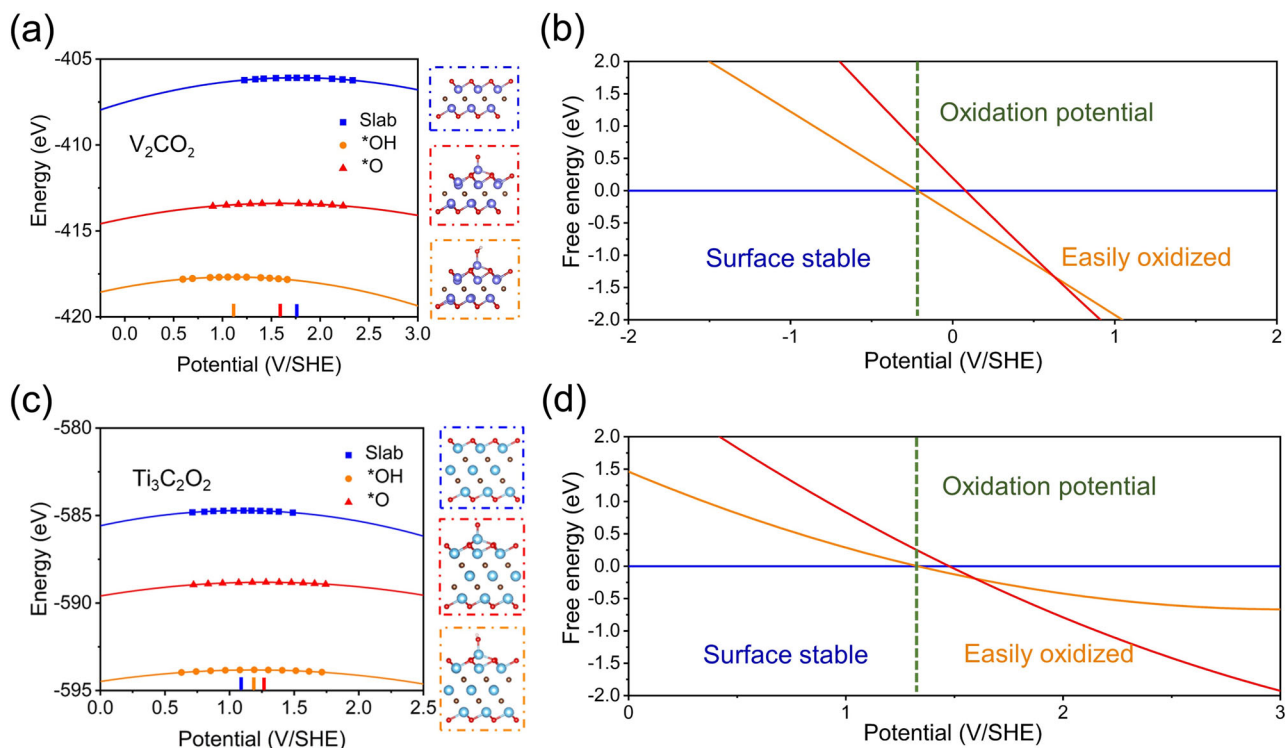
Fig. 4 | Thermodynamic analysis of oxidation process. The energies of the MXene slab (blue) and two oxidation states (*OH, yellow; *O, red) versus the electrode potential, (a) V_2CO_2 and (c) $Ti_3C_2O_2$. Symbols represent computationally derived values, and lines are fitted using a quadratic function ($E(U) = -\frac{1}{2}C(U - U_{PZC})^2 + E_{PZC}$). The potential of zero charge is marked with the short line. The free energies of the system as a function of potential, (b) V_2CO_2 and (d) $Ti_3C_2O_2$. Based on the free energy equation ($G_U(slab) + G(H_2O) \rightarrow G_U(*OH) + \frac{1}{2}G(H_2) + eU_{SHE} \rightarrow G_U(*O) + G(H_2) + 2eU_{SHE}$), the x-coordinate of the first intersection between the stable state (blue) and the oxidation states (*OH, yellow; *O, red) is marked as the oxidation potential with a green dashed line.
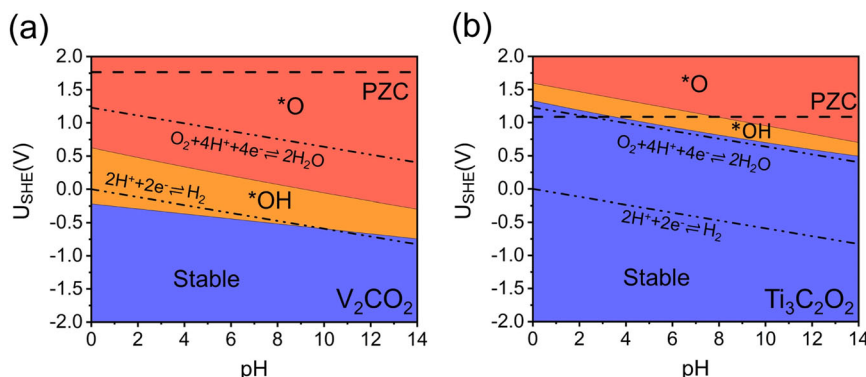

Fig. 5 | Pourbaix diagrams of oxidation. a V_2CO_2 and (**b**) $Ti_3C_2O_2$. The effect of pH on free energy was derived using the Nernst equation, $\triangle G_{pH} = -0.0592pH(eV)$, to determine the relationship between equilibrium potential and pH for each system. The stable state is represented in blue. The yellow and red represent different oxidation states. The dashed lines mark the position of the potential of zero charge (PZC). The two dash-dot-dot lines are reference lines of the reduction potentials of hydrogen and oxygen as reference, respectively.

needed to determine the role of defects in oxidation. Additionally, the oxidation behavior at the edges of MXenes is also an area that requires further theoretical investigation, as it may significantly influence the overall stability and performance of these materials.

Based on the above results, it is crucial for antioxidation purposes to minimize defects in MXenes through the utilization of optimal synthesis methods[31–33]. The Pourbaix diagrams for two perfect surface MXenes are shown in Fig. 5. In an OC state, they tend to exhibit a relatively high OC potential when in contact with an aqueous solution due to the low Fermi level of MXenes[34,35]. For instance, Fig. 5a, the OC potential of V_2CO_2 in pure water (which is equal to PZC) is 1.765 V, indicating its thermodynamic inclination towards spontaneous

oxidation. In contrast, Fig. 5b, $Ti_3C_2O_2$ benefits from its high oxidation potential and low PZC, rendering it more stable compared to V_2CO_2. This also explains why only one proton desorption occurs in the AIMD simulation of $Ti_3C_2O_2$ (Figure S3). Moreover, as pH increases, the difference between the oxidation potential and the PZC increases, leading to a stronger driving force for oxidation (Supplementary Figs. S20 and S21). This explains why MXenes are more prone to spontaneous oxidation under alkaline conditions[36,37].

In the presence of an external potential, the Pourbaix diagram can be used to evaluate the suitability of different MXenes for specific electrochemical applications. For example, when the blue region in Fig. 5a is below the oxygen redox potential and hydrogen reduction

Table 1 | Comparison of the oxidation potentials of various MXenes with respect to the standard hydrogen electrode (SHE)

Name	Oxidation potential (V vs. SHE)
V_2CO_2	−0.217
$V_4C_3O_2$	−0.075
Nb_2CO_2	−0.233
$Nb_4C_3O_2$	−0.054
$Ti_3C_2O_2$	1.329
$Ti_4C_3O_2$	1.575
Mo_2CO_2	2.524
$Mo_2TiC_2O_2$	2.550
$Mo_2Ti_2C_3O_2$	2.773

potential, the actual structure of MXenes as an oxygen or hydrogen electrocatalyst needs to be reevaluated. Although the oxidation of MXenes under reactive conditions does not necessarily impede the stable operation of MXene electrodes, neglecting this factor when designing electrode, especially in DFT-based research, may lead to significant discrepancies between theoretical predictions and actual performance[25]. Through the Pourbaix diagram, we also discovered the unique pH dependency of V_2CO_2, which becomes stable under alkaline hydrogen evolution potentials. This highlights the importance of using grand canonical energy calculations to uncover pH effects.

It should be noted that all the above discussions are based on the case of pure O termination. A major uncertainty in linking theoretical prediction of the MXene stability with the experiment is MXene termination, i.e., the composition of MXene surfaces. We have also studied the influence of different functional groups on the oxidation of MXenes. Supplementary Figs. S22, S23, and S24 illustrate the impact of the -OH functional group on the oxidation of MXenes. The -OH functional group can reduce the positive charge of surrounding metal atoms, act as a site being attacked, and lower the PZC, thereby protecting the surface. Additionally, the impact of OH functional groups becomes evident at low potentials[38]. Therefore, in predicting the properties of MXenes for specific applications, the primary functional groups under actual working conditions should be considered for a more accurate stability assessment.

Recently, the emergence of functional groups such as Cl, S, Se has provided new opportunities to address the challenge of MXenes' susceptibility to oxidation[1,39]. Taking V_2CCl_2 as an example (see Supplementary Figs. S25 and S26), the traditional F functional group is replaced by -O when in contact with water, consistent with previous studies[40]. However, we found that -Cl can still be stabilized at 1500 K. This is because the atomic radius of Cl is relatively large, providing ~1.7 Å of shielding distance and reducing the positive charge on the metal layer. Therefore, we consider functional group engineering as the most effective means to prevent the oxidation of MXene.

The subsequent calculations also include the determination of oxidation potentials for $V_4C_3O_2$, Nb_2CO_2, $Nb_4C_3O_2$, $Ti_4C_3O_2$, Mo_2CO_2, $Mo_2TiC_2O_2$, and $Mo_2Ti_2C_3O_2$, and the results are shown in Table 1. It is observed that in MXenes composed of the same elements, as the value of n in $(M_{n+1}X_nT_x)$ increases, the oxidation potential tends to rise. For instance, $V_4C_3O_2$ exhibits an oxidation potential of −0.075 V, -0.2 V higher than that of V_2CO_2. However, this increase in potential cannot offset the differences caused by the type of elements. Mo_2CO_2 demonstrates a remarkably high oxidation potential of 2.524 V. The van der Waals surface electrostatic potential maps also indicate that Mo_2CO_2 is more resistant to nucleophilic attack, as shown in Supplementary Fig. S27. In fact, Mo_2C is indeed more stable than Ti_3C_2[41]. In addition, the basal plane chemistry of double transition metal MXenes is dominated by the outermost metal[42]. When Mo is used as the outermost layer of double-transition metal MXenes, it shows high

oxidation potentials. For instance, $Mo_2TiC_2O_2$ has an oxidation potential of 2.550 V. This also provides an idea for the design of anti-oxidant MXenes.

Besides the factors discussed above, the oxidation potentials of MXenes are also influenced by the solution environment. For instance, the presence of hydrated cations reduces the amount of free surface water, leading to a significant increase in the working potential of MXenes in high-concentration salt solutions[13,43].

Oxidation/reconstruction of non-MXene materials

It is worth noting that the oxidation mechanism discovered in this work is not exclusive to MXenes. MBenes, as boron analogs of MXenes, have the potential to dissolve in water and undergo nonclassical crystallization, leading to structural alterations[44]. Similar to MXenes, MBenes exhibit O-functionalization as the primary mechanism under high potential[45], and O-functionalized MBenes also possess very high work functions ($Mo_2B_2O_2$: 7.25 eV)[22]. We observed a similar water attack behavior in $Mo_2B_2O_2$ (see Supplementary Fig. S28), suggesting that the structural changes due to the OER-like reaction may also exist in other materials.

Notably, the generation of metal oxides under high electrode potential is a common occurrence for transition metal non-oxides[46–49], especially when the potential exceeds 1.23 V[50], implying that the restructuring of some catalysts during the catalytic process may be induced by the OER reaction. Recent studies have also documented similar corrosion (reconstruction) behaviors in oxides[51,52], further underscoring the widespread implications of the OER-like mechanism. Additionally, recent research has shown that CO-induced roughening of Cu surfaces is also a Walden-type inversion[53], suggesting that the Walden inversion is not limited to the OER-like mechanism. Based on these phenomena, we speculate that Walden inversion may be broadly present in molecule-induced material reconstruction. Specifically, when metal atoms are present in the subsurface layer, they are likely to serve as sites for backside attacks by molecules, thereby inducing structural changes.

Therefore, due to the universality of the oxidation (corrosion/reconstruction) phenomenon, the findings of this study not only contribute to the understanding of MXene oxidation but also present a viable avenue for exploring the stability of catalysts under practical working conditions.

Discussion

We investigated the oxidation behavior of MXenes using the CP-HS-DM model and found a strong correlation between the oxidation state of metal atoms and the oxidation state of oxygen atoms in water molecules. The reaction mechanism bears similarity to that of the OER, exhibiting clear potential dependence. Utilizing the constant-potential implicit solvent model, we investigated the oxidation potentials of common MXenes and studied the impact of structural factors such as defect functional groups on oxidation. We discovered that the high PZC is a crucial factor contributing to the spontaneous oxidation of MXenes in aqueous solutions. To enhance the stability of MXenes, it is crucial to employ effective synthesis methods to minimize defect formation. Furthermore, functional group engineering offers additional possibilities for antioxidation. Notably, the structural changes induced by molecule attacks are not exclusive to MXenes, as similar phenomena are observed in MBenes, metal oxides, and even on copper surfaces. This theoretical work provides insights and viable approaches for corrosion research and anti-corrosion design of MXenes and other electrode materials.

Methods

Model set-up of the MXene−water interfaces

In the simulations, we used two kinds of MXene-water interface models. All models had an average water density of ~1 g/ml. To

investigate the oxidation process of MXenes, we adopted the confined water model (Supplementary Fig. S1a). This choice was based on our previous demonstration that the oxidation mechanisms between bulk water and confined water environments are similar[9]. Selecting the confined water model helps to speed up simulations. For exploring the influence of electrode potential, we used the bulk water model (Supplementary Fig. S1b) to apply the potential.

All oxygen-containing models were built by adding an oxygen molecule to these two models. In the confined water model, the oxygen concentration was ~3 M, and in the bulk water model, it was about 2 M. Although this concentration is much higher than the natural concentration of dissolved oxygen, it is realistic for oxygen-related applications.

DFT settings of static and dynamic calculations

All calculations were carried out using density functional theory (DFT) implemented through the Vienna ab initio Simulation Package[54,55]. The Perdew-Burke-Ernzerhof (PBE) functional, together with D3 van der Waals correction, was employed in all calculations[56–58]. The plane-wave basis cutoff energy is set to 500 eV for all simulations. A $3 \times 3 \times 1$ gamma-centered k-mesh was used in the relaxation, while the gamma point of the Brillouin zone, with no consideration of symmetry, was adopted in the ab initio molecular dynamic (AIMD) simulations. The time step in all AIMD simulations was set to be 1.0 femtosecond, and the Nose-Hoover thermostat[59] was used to maintain the system temperature. Some of the data are processed using vaspkit[60]. The surface electrostatic potential data were processed using VESTA[61].

Constrained ab initio molecular dynamic simulation

The "slow-growth" approach[62] was adopted, as implemented in VASP, to obtain the changes in free energy during the reaction process. In this method, a suitable collective variable (CV), namely ε, can be selected as the reaction coordinate, which is linearly changed from the initial state to the final state at a transformation velocity $\dot{\varepsilon}$. The work needed to accomplish the transformation from the initial to final states can be calculated as follows:

$$W_{Is-Fs} = \int_{\varepsilon(Is)}^{\varepsilon(Fs)} \left(\frac{\partial F}{\partial \varepsilon}\right) \cdot \dot{\varepsilon} dt \qquad (4)$$

Where F is the evolving free energy with respect to time. The partial derivative of F with respect to ε, $(\frac{\partial F}{\partial \varepsilon})$, is computed during constrained ab initio molecular dynamics (cAIMD) using the blue-moon ensemble implemented with the SHAKE algorithm[63]. Given the infinitesimally small nature $\partial \varepsilon$, the needed work (W_{Is-Fs}) corresponds to the difference in free energy between the initial and final states. For the "slow-growth" sampling, a value of 0.0005 Å for $\partial \varepsilon$ is employed for each cAIMD step, determined after testing the effectiveness of a shorter step size. The selected CV for this study is illustrated in Figure S6.

Constant-potential hybrid-solvation dynamic model

A constant-potential hybrid-solvation dynamic model (CP-HS-DM)[17–19] was used to implement the addition of constant potential to the dynamic process. Under this model, the solvent effect of the system is described using both explicit and implicit solvents. The electrons are regulated by a fictitious constant potentiometer[64], causing the system potential (U_{SHE}) to fluctuate at a preset potential. Where U_{SHE} is defined by the following equation:

$$U_{SHE} = -4.6V + \phi_q/e \qquad (5)$$

Where ϕ_q represents the work function of the system when the electrolyte potential is zero. 4.6 V is the absolute electrode potential of the SHE benchmarked in VASPsol[65]. In the ab initio molecular dynamics at a

constant-potential, we adjust the electron number every 10 MD steps to correct the potential. At this point, VASPsol will be turned on to calculate the system work function and keep the total system charge neutral. The effective surface tension parameter was assigned to 0 in VASPsol to neglect the cavitation energy contribution. The linearized Poisson–Boltzmann model with a Debye length of 3.04 Å mimics the compensating charge and the relative permittivity was set to 78.4 to model the aqueous electrolyte. The validity of the model can be referred to Fig. 2d.

Grand canonical free energy

The double-reference method was employed to model the electrochemical metal/solution interface and to evaluate the influence of solvation and the applied potential on the reaction energetics[20,28,66–68]. The aqueous environment in this part is modeled as a continuum dielectric as implemented also by VASPsol with the same settings as the CP-HS-DM. The grand canonical energy (E) of the system is defined by the following equation:

$$E = E_{DFT} - \Delta n(V_{sol} - \phi_q/e) \qquad (6)$$

Where E_{DFT} is the DFT-calculated energy and V_{sol} is the electrostatic potential of the bulk electrolyte.

For each structure, we varied the excess charge of the unit cell (Δn) from -0.5 e to $+0.5$ e in steps of 0.1 e. The energy at different charge values is then fitted as a quadratic function of the potential dependence[69], as shown in the following equations:

$$E(U) = -\frac{1}{2}C(U - U_{PZC})^2 + E_{PZC} \qquad (7)$$

Where C, U_{PZC}, and E_{PZC} are the fitted values of the potential of zero charge (PZC), capacitance of the corresponding system, and the energy of the system at the PZC, respectively. The grand canonical free energy $G(U)$ related to the potential can be obtained from the following equation.

$$G(U) = E(U) + ZPE - TS \qquad (8)$$

Therefore, based on the fitted quadratic function, we can obtain the grand canonical free energy at both ends of the redox reaction as a function of potential.

Reporting summary

Further information on research design is available in the Nature Portfolio Reporting Summary linked to this article.

Data availability

The data supporting the findings of this study have been included in the main text and Supplementary Information. The structure models used are provided in Supplementary Data 1. Source data are provided with this paper.

References

1. Cao, F. et al. Recent advances in oxidation stable chemistry of 2D MXenes. *Adv Mater* **34**, e2107554 (2022).
2. Averbeck, S. R. et al. Stability of Ti₃C₂Tₓ MXene films and devices under clinical sterilization processes. *ACS Nano* **17**, 9442–9454 (2023).
3. Narayanasamy, M. et al. Morphology restrained growth of V₂O₅ by the oxidation of V-MXenes as a fast diffusion controlled cathode material for aqueous zinc ion batteries. *Chem Commun (Camb)* **56**, 6412–6415 (2020).
4. Saraf, M. et al. Enhancing charge storage of Mo₂Ti₂C₃ MXene by partial oxidation. *Adv.Funct. Mater.* **34**, 2306815 (2023).

5. Huang, S. & Mochalin, V. N. Hydrolysis of 2D transition-metal carbides (MXenes) in colloidal solutions. *Inorg Chem* **58**, 1958–1966 (2019).
6. Zhang, C. J. et al. Oxidation stability of colloidal two-dimensional titanium carbides (MXenes). *Chemistry of Materials* **29**, 4848–4856 (2017).
7. Natu, V. et al. Edge capping of 2D-MXene sheets with polyanionic salts to mitigate oxidation in aqueous colloidal suspensions. *Angew Chem Int Ed Engl* **58**, 12655–12660 (2019).
8. Lotfi, R., Naguib, M., Yilmaz, D. E., Nanda, J. & van Duin, A. C. T. A comparative study on the oxidation of two-dimensional Ti_3C_2 MXene structures in different environments. *Journal of Materials Chemistry A* **6**, 12733–12743 (2018).
9. Hou, P. et al. Unraveling the oxidation behaviors of MXenes in aqueous systems by active-learning-potential molecular-dynamics simulation. *Angew Chem Int Ed Engl* **62**, e202304205 (2023).
10. Wu, T., Kent, P. R. C., Gogotsi, Y. & Jiang, D. e. How water attacks MXene. *Chemistry of Materials* **34**, 4975–4982 (2022).
11. Hou, P. et al. Proton-driven dynamic behavior of nanoconfined water in hydrophilic MXene sheets. *Angew Chem Int Ed Engl*, e202411849 https://doi.org/10.1002/anie.202411849 (2024).
12. Wang, X. et al. Titanium carbide mxene shows an electrochemical anomaly in water-in-salt electrolytes. *ACS Nano* **15**, 15274–15284 (2021).
13. Zhu, Y. et al. Kinetic regulation of MXene with water-in-LiCl electrolyte for high-voltage micro-supercapacitors. *Natl Sci Rev* **9**, nwac024 (2022).
14. Tang, J. et al. Tuning the electrochemical performance of titanium carbide MXene by controllable in situ anodic oxidation. *Angewandte Chemie* **131**, 18013–18019 (2019).
15. Tan, Z.-L. et al. V_2CT_x MXene and its derivatives: synthesis and recent progress in electrochemical energy storage applications. *Rare Metals* **41**, 775–797 (2021).
16. Shan, Q. et al. Two-dimensional vanadium carbide (V_2C) MXene as electrode for supercapacitors with aqueous electrolytes. *Electrochemistry Communications* **96**, 103–107 (2018).
17. Zhao, X. & Liu, Y. Origin of selective production of hydrogen peroxide by electrochemical oxygen reduction. *J Am Chem Soc* **143**, 9423–9428 (2021).
18. Yu, S., Levell, Z., Jiang, Z., Zhao, X. & Liu, Y. What is the rate-limiting step of oxygen reduction reaction on Fe-N-C catalysts? *J Am Chem. Soc.* **145**, 25352–25356 (2023).
19. Bai, X. et al. Dynamic stability of copper single-atom catalysts under working conditions. *J Am Chem Soc* **144**, 17140–17148 (2022).
20. Hu, X. et al. What is the real origin of the activity of Fe-N-C electrocatalysts in the O_2 reduction reaction? critical roles of coordinating pyrrolic N and axially adsorbing species. *J Am Chem Soc* **144**, 18144–18152 (2022).
21. Alameda, L. T., Moradifar, P., Metzger, Z. P., Alem, N. & Schaak, R. E. Topochemical deintercalation of Al from MoAlB: stepwise etching pathway, layered intergrowth structures, and two-dimensional MBene. *J Am Chem Soc* **140**, 8833–8840 (2018).
22. Hou, P. et al. P-type ohmic contacts of MBenes with MoS_2 for nanodevices and logic circuits. *2D Materials* **9**, 045022 (2022).
23. Zhang, H., Zhu, M. & Zheng, Y. First principles study on the intrinsic resistivity of rectangular Ti_2B_2 and Mo_2B_2. *Phys. Rev. B* **108**, 245425 (2023).
24. Naguib, M., Unocic, R. R., Armstrong, B. L. & Nanda, J. Large-scale delamination of multi-layers transition metal carbides and carbonitrides "MXenes". *Dalton Trans* **44**, 9353–9358 (2015).
25. Kuznetsov, D. A. et al. Single-atom-substituted Mo_2CT_x:Fe-layered carbide for selective oxygen reduction to hydrogen peroxide: tracking the evolution of the MXene phase. *J Am Chem Soc* **143**, 5771–5778 (2021).
26. Lukatskaya, M. R. et al. Cation intercalation and high volumetric capacitance of two-dimensional titanium carbide. *Science* **341**, 1502–1505 (2013).
27. Hu, P. et al. Vanadium oxide: phase diagrams, structures, synthesis, and applications. *Chem Rev* **123**, 4353–4415 (2023).
28. Taylor, C. D., Wasileski, S. A., Filhol, J.-S. & Neurock, M. First principles reaction modeling of the electrochemical interface: consideration and calculation of a tunable surface potential from atomic and electronic structure. *Phys. Rev. B.* **73**, 165402 (2006).
29. Zhan, C. et al. Understanding the MXene pseudocapacitance. *J Phys Chem Lett* **9**, 1223–1228 (2018).
30. Michalowski, P. P. et al. Oxycarbide MXenes and MAX phases identification using monoatomic layer-by-layer analysis with ultralow-energy secondary-ion mass spectrometry. *Nat Nanotechnol* **17**, 1192–1197 (2022).
31. Sarycheva, A., Shanmugasundaram, M., Krayev, A. & Gogotsi, Y. Tip-Enhanced Raman Scattering Imaging of Single- to Few-Layer $Ti_3C_2T_x$ MXene. *ACS Nano* **16**, 6858–6865 (2022).
32. Mathis, T. S. et al. Modified MAX phase synthesis for environmentally stable and highly conductive Ti_3C_2 MXene. *ACS Nano* **15**, 6420–6429 (2021).
33. Li, X. et al. Ambient-stable MXene with superior performance suitable for widespread applications. *J. Chem. Eng.* **455**, 140635 (2023).
34. Andersson, L. & Zhang, C. Molecular dynamics simulations of metal-electrolyte interfaces under potential control. *Curr. Opin. Electrochem.* **42**, 101407 (2023).
35. Boettcher, S. W. et al. Potentially confusing: potentials in electrochemistry. *ACS Energy Letters* **6**, 261–266 (2020).
36. Zhao, Y. et al. Engineering strategies and active site identification of MXene-based catalysts for electrochemical conversion reactions. *Chem. Soc. Rev.* **52**, 3215–3264 (2023).
37. Zhao, X. et al. pH, nanosheet concentration, and antioxidant affect the oxidation of $Ti_3C_2T_x$ and Ti_2CT_x MXene dispersions. *Adv. Mater. Interfaces* **7**, 2000845 (2020).
38. Gao, G., O'Mullane, A. P. & Du, A. 2D MXenes: a new family of promising catalysts for the hydrogen evolution reaction. *ACS Catalysis* **7**, 494–500 (2016).
39. Kamysbayev, V. et al. Covalent surface modifications and superconductivity of two-dimensional metal carbide MXenes. *Science* **369**, 979–983 (2020).
40. Xie, Y. et al. Role of surface structure on Li-ion energy storage capacity of two-dimensional transition-metal carbides. *J Am Chem Soc* **136**, 6385–6394 (2014).
41. Guo, Y. et al. Synthesis of two-dimensional carbide Mo_2CT_x MXene by hydrothermal etching with fluorides and its thermal stability. *Ceramics International* **46**, 19550–19556 (2020).
42. Jin, D. et al. Computational screening of 2D ordered double transition-metal carbides (MXenes) as Electrocatalysts for hydrogen evolution reaction. *J. Phys. Chem. C* **124**, 10584–10592 (2020).
43. Li, X. et al. Intrinsic voltage plateau of a Nb_2CT_x MXene cathode in an aqueous electrolyte induced by high-voltage scanning. *Joule* **5**, 2993–3005 (2021).
44. Gunda, H. et al. Progress, challenges, and opportunities in the synthesis, characterization, and application of metal-boride-derived two-dimensional nanostructures. *ACS Mater. Lett.* **3**, 535–556 (2021).
45. Zhu, X., Zhou, X., Jing, Y. & Li, Y. Electrochemical synthesis of urea on MBenes. *Nat Commun* **12**, 4080 (2021).
46. Wygant, B. R., Kawashima, K. & Mullins, C. B. Catalyst or precatalyst? the effect of oxidation on transition metal carbide, pnictide, and chalcogenide oxygen evolution catalysts. *ACS Energy Lett.* **3**, 2956–2966 (2018).
47. Fan, K. et al. Direct observation of structural evolution of metal chalcogenide in electrocatalytic water oxidation. *ACS Nano* **12**, 12369–12379 (2018).

48. Wu, Q. et al. Non-covalent ligand-oxide interaction promotes oxygen evolution. *Nat Commun* **14**, 997 (2023).
49. Hu, Y. et al. Understanding the sulphur-oxygen exchange process of metal sulphides prior to oxygen evolution reaction. *Nat Commun* **14**, 1949 (2023).
50. Xu, J. & Peng, Z. Redox chemistry in solid catalysts for regulating oxygen electrode working mechanism in aqueous electrolytes, what's next? *Next Materials* **1**, 100006 (2023).
51. Hess, F. & Over, H. Coordination inversion of the tetrahedrally coordinated Ru_4f surface complex on $RuO_2(100)$ and its decisive role in the anodic corrosion process. *ACS Catalysis* **13**, 3433–3443 (2023).
52. Ju, M. et al. Fe(III) docking-activated sites in layered birnessite for efficient water oxidation. *J Am Chem Soc* **145**, 11215–11226 (2023).
53. Zhang, Z., Gee, W., Sautet, P. & Alexandrova, A. N. H and CO Co-induced roughening of Cu surface in CO_2 electroreduction conditions. *J Am Chem Soc* **146**, 16119–16127 (2024).
54. Kresse, G. & Hafner, J. Ab initio molecular dynamics for liquid metals. *Phys Rev B Condens Matter* **47**, 558–561 (1993).
55. Kresse, G. & Furthmüller, J. Efficiency of ab-initio total energy calculations for metals and semiconductors using a plane-wave basis set. *Comput. Mater. Sci.* **6**, 15–50 (1996).
56. Grimme, S., Antony, J., Ehrlich, S. & Krieg, H. A consistent and accurate ab initio parametrization of density functional dispersion correction (DFT-D) for the 94 elements H-Pu. *J Chem Phys* **132**, 154104 (2010).
57. Hu, X. et al. Understanding the role of axial O in CO_2 electroreduction on NiN_4 single-atom catalysts via simulations in realistic electrochemical environment. *J. Mater. Chem. A* **9**, 23515–23521 (2021).
58. Tian, Y. et al. A general strategy to stabilize $1T-MoS_2$ using MXene heterostructures and unlock its hydrogen evolution reaction capabilities. *Phys Chem Chem Phys* **25**, 27181–27188 (2023).
59. Braga, C. & Travis, K. P. A configurational temperature Nose-Hoover thermostat. *J Chem Phys* **123**, 134101 (2005).
60. Wang, V., Xu, N., Liu, J.-C., Tang, G. & Geng, W.-T. VASPKIT: a user-friendly interface facilitating high-throughput computing and analysis using VASP code. *Comput. Phys. Commun.* **267**, 108033 (2021).
61. Momma, K. & Izumi, F. VESTA 3 for three-dimensional visualization of crystal, volumetric and morphology data. *J. Appl. Crystallogr.* **44**, 1272–1276 (2011).
62. Woo, T. K., Margl, P. M., Blöchl, P. E. & Ziegler, T. A combined car–parrinello QM/MM implementation for ab Initio molecular dynamics simulations of extended systems: application to transition metal catalysis. *J. Phys. Chem. B* **101**, 7877–7880 (1997).
63. Sprik, M. & Ciccotti, G. Free energy from constrained molecular dynamics. *J. Chem. Phys.* **109**, 7737–7744 (1998).
64. Bonnet, N., Morishita, T., Sugino, O. & Otani, M. First-principles molecular dynamics at a constant electrode potential. *Phys Rev Lett* **109**, 266101 (2012).
65. Mathew, K., Kolluru, V. S. C., Mula, S., Steinmann, S. N. & Hennig, R. G. Implicit self-consistent electrolyte model in plane-wave density-functional theory. *J Chem Phys.* **151**, 234101 (2019).
66. Duan, Z. & Henkelman, G. Theoretical resolution of the exceptional oxygen reduction activity of au(100) in alkaline media. *ACS Catalysis* **9**, 5567–5573 (2019).
67. Kopac Lautar, A. et al. Electrolyte reactivity in the double layer in Mg batteries: an interface potential-dependent DFT study. *J Am Chem Soc* **142**, 5146–5153 (2020).
68. Filhol, J.-S. & Neurock, M. Elucidation of the electrochemical activation of water over Pd by first principles. *Angewandte Chemie.* **118**, 416–420 (2006).
69. Ringe, S., Hormann, N. G., Oberhofer, H. & Reuter, K. Implicit solvation methods for catalysis at electrified interfaces. *Chem Rev.* **122**, 10777–10820 (2022).

Author contributions

Y.T. and X.M. conceived and designed the project. Y.T., P.H., and H.Z. wrote the manuscript. Q.L., Y.T., A.V., and J.W. analyzed the results. Q.L., Y.X., G.C., and F.D. reviewed and edited the manuscript. All authors contributed towards discussion on the manuscript.

Competing interests

The authors declare no competing interests.

Additional information

Supplementary information The online version contains supplementary material available at https://doi.org/10.1038/s41467-024-54455-z.

Correspondence and requests for materials should be addressed to Quan Li, Fei Du, Aleksandra Vojvodic, Jianzhong Wu or Xing Meng.

Peer review information *Nature Communications* thanks Kai S. Exner, and the other anonymous reviewer(s) for their contribution to the peer review of this work. A peer review file is available.

Reprints and permissions information is available at http://www.nature.com/reprints

Publisher's note Springer Nature remains neutral with regard to jurisdictional claims in published maps and institutional affiliations.